Journal of Marine Science and Application (2024) 23: 734-742
https://doi.org/10.1007/s11804-024-00432-3

RESEARCH ARTICLE

Experimental Investigation of Water Entry Flow and Impact Load Characteristics of Northern Gannet's Head

Le Shen[1,2], Yunhua Jiang[1,3], Hanrui Wang[1], Zhihui Zou[1] and Zhenjiang Wang[1]

Received: 12 May 2023 / Accepted: 20 August 2023

Abstract
To explore the water entry flow and impact load characteristics of northern gannets, we conducted water entry experiments using a northern gannet's head model based on three-dimensional (3D) printing and several cone models under different Froude numbers. A high-speed camera was used to capture flow images, and an inertial measurement unit (IMU) was used to record the water entry impact loads. The results indicate that the geometric topology of the model considerably influenced the water entry flow and impact load. Specifically, the northern gannet's head model created a smaller water entry splash crown, cavity geometry, and impact load compared with the cone models of similar sizes.

Keywords Northern gannet; Cone models; Water entry; Splash crown; Cavity evolution; Impact load

1 Introduction

Northern gannets comprise a type of plunge-diving bird. These animals can dive at speeds of up to 24 m/s (the hypothetical maximum diving speed reaches as high as 80 m/s) and catch fish at depths of 10–20 m without incurring injuries (Bush and Hu, 2006; Garthe et al., 2000; Bhar et al., 2019; Pandey et al., 2022). Northern gannets adjust their dive based on the depth of their prey. Specifically, they perform a V-shaped dive, with a short entry period, and strike the water surface at an angle when their prey is at shallow depths; they perform a U-shaped dive, which requires a long entry period when their prey is found at great depths (Capuska et al., 2011; Capuska et al., 2013). Moreover, to reduce high-speed water entry impact load, northern gannets fold their wings and straighten their necks to reduce the contact area with water (Lee and Reddish, 1981; Low et al., 2015). Ropert-Coudert et al. (2004) used acceleration data loggers to record the acceleration and entry depth data on the water entry of natural gannets. The recorded data show that the gannets used their momentum to travel underwater at an average descent rate of 2.87 m/s (s_d=±1.53) and actively made a brake after reaching the desired depth (range: 0.3–9.7 m). During high-speed plunge diving (i.e., most gannets plunge from a height of approximately 30 m), the peak impact acceleration of gannets, which exerts a considerable force on their body, can reach around 23 times the gravitational acceleration based on numerical simulation (Yang et al., 2012; Wang et al., 2013). The pressure distribution on the gannet's body surface under various water entry angles indicates that a large pressure asymmetry caused by a small water entry angle may lead to a large impact action on the longitudinal body axis and damage the animal's neck. These findings partly explain the water entry of gannets at a large water entry angle from the perspective of impact mechanics (Yang et al., 2012; Wang et al., 2013). Liang et al. (2013) developed a bionic gannet to investigate the impact load of water entry based on the analysis of body configu-

Article Highlights

- A series of water entry experiments of the northern gannet's head model based on the 3D print and some cone models are performed under different Froude numbers. The flow images are captured by a high-speed camera and the water entry impact loads are recorded by an inertial measurement unit.
- The water entry splash crown and cavity geometry created by the northern gannet's head model are smaller than the ones created by the same size and close size cone models.
- The water entry impact load of the northern gannet's head model is also smaller than the ones caused by the same size and close size cone models.

✉ Yunhua Jiang
jiangyh35@mail.sysu.edu.cn

[1] School of Ocean Engineering and Technology, Sun Yat-sen University & Southern Marine Science and Engineering Guangdong Laboratory (Zhuhai), Zhuhai 519000, China

[2] School of Naval Architecture, Ocean & Civil Engineering, Shanghai Jiao Tong University, Shanghai 200240, China

[3] Key Laboratory of Comprehensive Observation of Polar Environment (Sun Yat-sen University), Ministry of Education, Zhuhai 519082, China

ration and skeleton structure and motion patterns of gannet wings during plunge diving. Their prototype was equipped with adjustable sweptback wings to adopt various body shapes for water entry. The maximum peak impact acceleration and overload reached 167.20 m/s^2 and 18.06, respectively.

Seabirds experience no injuries during high-speed plunge diving. To clarify the underlying mechanical mechanism, some studies have focused on water entry cavity flow characteristics and impact loads of gannets. Chang et al. (2016) used the buckling and nonbuckling behaviors of an elastic beam to represent the stability of seabirds' necks; they modeled the gannet neck as an elastic beam and replaced the gannet head with a cone model. In addition, they explored the effect of neck muscles on the modification of the buckling criterion. As shown by the results based on a force transducer, plunge-diving seabirds possess a unique morphology, dive at appropriate speeds, and have strong neck muscles for safe diving at high speeds.

The neck and body of a gannet were represented by a gannet-inspired system modeled as an Euler–Bernoulli or Timoshenko beam. Meanwhile, cones with varying half-angles were used to model the gannet head. The results show that the critical velocity was the greatest under clamped–clamped boundary conditions due to the increased stability at both ends of the beam. Furthermore, the softening of joints during plunge diving consistently decreased the buckling speed of the system and considerably altered the buckling shape (Zimmerman et al., 2019; Zimmerman and Abdelkefi, 2020a; 2020b).

Sharker et al. (2019) recreated a gannet model with a mass of 0.452 kg via three-dimensional (3D) printing and measured the impact acceleration of water entry using an embedded inertial measurement unit (IMU) with impact velocities ranging from 4.4 to 23.2 m/s. The plunge-diving bird (northern gannet) attained the highest acceleration, which was approximately 25 times the gravitation acceleration. Thus, based on human injury data, the destructive effect of sudden changes in motion occurs observed below the theoretical safety limit, i. e., the nondimensionalizing jerk value ($J^* = \frac{\Delta a}{\Delta t} \cdot \frac{m}{0.5\rho g U A}$). Here, Δa refers to acceleration change during impact, Δt denotes the impact duration, m indicates the total mass of the real bird, ρ represents water density, U means the impact velocity, and A is the cross-sectional area of the bird neck.

Furthermore, a plunge dive involves three notable phases: 1) impact phase, 2) air cavity phase, and 3) submerged phase. A greater risk of bird neck injury can be observed during the impact and air cavity phases than during the submerged phase. The force is spread along the feather pattern, that is, over a considerably large area of the body, before being transferred to the skin, which reduces the pressure on the skin after the pinch-off based on the hypothesis introduced in the work of Bhar et al. (2019). Moreover, the impact dynamics of animal (i. e., dolphins, plunge-diving gannets, and water-walking basilisk lizards) and human diving (i.e., diving head first, diving hand first, and diving feet first) were investigated (Pandey et al., 2022). The dimensionless time-averaged impulse versus the diving height plot was used to propose a safe height for human diving in a particular body position (Pandey et al., 2022).

In addition, water entry is a fundamental and prevalent problem in different applications (Jiang et al., 2018a; Jiang et al., 2018b; Jiang et al., 2021). This condition includes natural phenomena, such as a basilisk lizard walking on the water surface (Glasheen and McMahon, 1996) and a stone skipping on water (Clanet et al., 2004); military applications, such as antitorpedo and antisubmarine water entry (May, 1975); aerospace engineering applications, such as the water entry impact of aerospace structures (Seddon and Moatamedi, 2006); sports applications, such as the water entry of swimmers and divers and the entry and exit of oars during rowing (Truscott et al., 2014). Object water entry is accompanied by three main scientific problems: impact load prediction, calculation of vehicle trajectory with cavity running, and comprehension of air cavity development.

Based on previous studies, this study aimed to determine the impact load of water entry differences between a northern gannet's head and cone models with the same cone angle as the northern gannet's head. Therefore, water entry flow and impact load characteristics of northern gannets were experimentally investigated using a series of water entry experiments on northern gannets' head model based on 3D printing and different cone models under various Froude numbers. The rest of this paper is organized as follows: Section 2 provides details on the experimental methodology. Section 3 presents the experimental observations on water entry for different models, cavity characteristics, and water entry load properties under various Froude numbers. Section 4 presents the conclusions.

2 Experimental setup

Systematic experiments were conducted to investigate the flow and load characteristics of the northern-gannet head model as it penetrates the air–water interface. Experiments were performed in a water entry experimental system, which mainly comprised a water tank, a high-speed imaging system, an IMU, a model release system, and the experimental models (Figure 1).

The water tank consisted of a tempered glass water tank with dimensions of 1 800 mm×800 mm×1 000 mm and a wall thickness of 15 mm. The plastic elastic mesh frame set at the bottom of the water tank prevented the model from hitting it. The high-speed imaging system comprised a Photron Fastcam Mini AX200 high-speed camera and a 3×4 100 W light-emitting diode (LED) light array. Uniform

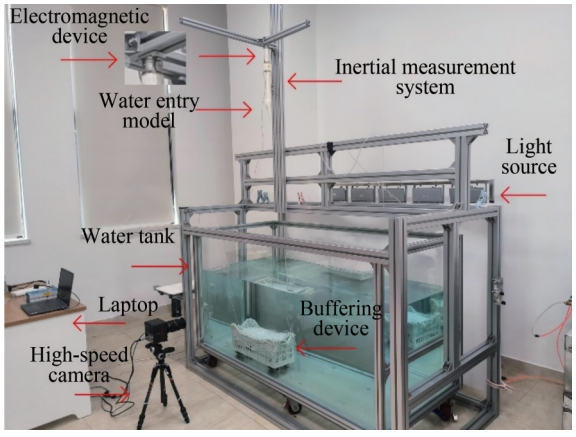

Figure 1 Schematic of water entry experimental setup

light and clear image capture, were ensured by covering the LED light source with a piece of white plastic sheet. The IMU comprised a microcontroller, an MPU6500 motion tracking device, and a W25Qxxx series memory unit. The microcontroller was equipped with an Arduino control board, and the MPU6500 accelerometer was sampled at 4 000 Hz in the measurement range of ±16 g. Given the data storage, a sampling frequency of 1 250 Hz was used. The IMU was embedded in the tail of the bird head and cone models during each test to record instantaneous impact events, which were stored in the electromagnetic device to achieve the free release of the model. Acceleration had a measurement uncertainty of 3%.

The experimental models included the northern gannet head model and four cone models using ordinary resin. The geometry of the bird head model was obtained via the reversal of the 1∶1 image of the 2D gannet specimen and its conversion to 3D format (Chang et al., 2016). To compare the water entry characteristics of the bird head and cone models, we designed four cone models with various maximum cross-sectional sizes.

Specifically, the cone angles (i.e., $\alpha = 7.9°, \beta = 12.3°$) and total length ($L_M = 156.2$ mm) of the cone models were kept the same as those of the bird head model (Figure 2). However, the maximum cross-sectional area was set to be greater than, equal to, and less than the cross-sectional area of the bird head model. Using the radius of their maximum cross-sectional area, the cone models were named cones R24, R23.5, R21.5, and R19.5. Cone R23.5 and the bird head model had the same maximum cross-sectional area (i.e., 1 713 mm^2). In addition, the diameter of cone R24 was the same as the maximum diameter of the bird head model because the bird head is not a regular circle (Figures 2(a)–2(b)).

The bird head and cone models showed slightly different masses. Specifically, the bird head model and cones R24, R23.5, R21.5, and R19.5 had masses of 0.510, 0.493, 0.492, 0.489, and 0.475 kg, respectively. These models exhibited a maximum mass difference of 0.035 kg. To clarify

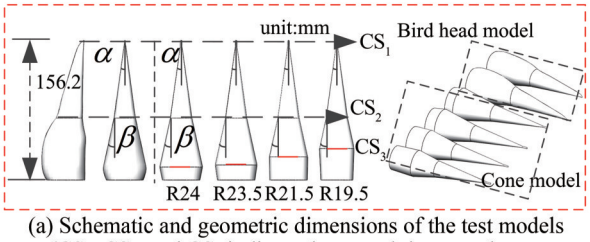

(a) Schematic and geometric dimensions of the test models (CS_1, CS_2, and CS_3 indicate the rostral tip, rostral root, and maximum cross-section of the models, respectively)

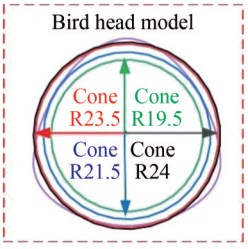

(b) Comparison of maximum cross-sections of the different models (The purple, green, blue, red and black graphics represent the bird head, Cone R19.5, Cone R21.5, Cone R23.5 and Cone R24 respectively)

Figure 2 Three-dimensional and two-dimensional schematics of bird head and cone models

the effects of mass difference on impact load, we performed comparison experiments on all the cone models having the original mass and the same mass as the bird head model (i.e., 0.510 kg) at three different release heights. Figure 3 presents the impact load results ($H = 122$ cm) of the cone models with the original mass and the same mass as the bird head model. The various model masses resulted in a considerably small impact load difference. The main dimensionless number is the Froude number, which is defined as $Fr = \frac{U}{\sqrt{g d_{CS_3}}}$ and ranged from 4.97 to 7.18 (i.e., Fr of the bird head model). Here, g refers to the gravitational acceleration, U denotes the water entry velocity of the model, and d_{CS_3} indicates the location diameter CS_3 (i.e., maximum cross-section). Experiments were conducted at least thrice to meet data repeatability requirements (Figure 4).

3 Experimental results

3.1 Water entry cavity flow

To investigate the water entry cavity of the bird head and cone models, we performed experiments under different release heights (52, 87, and 122 cm) and based on experimental equipment and facilities available in the laboratory. For comparison, the typical water entry cavity images of the bird head and cone models under the same release height (122 cm from the water surface) were obtained (Figures 5–9). The water entry cavity flow caused by the bird head and cone models was the same as that observed in previous studies

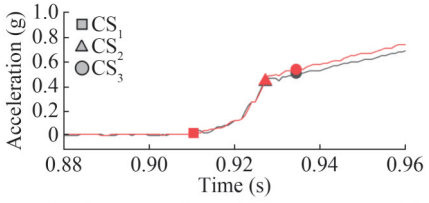

(a) The comparison of Cone R19.5 models

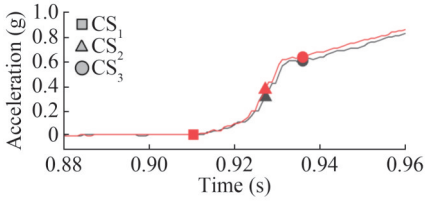

(b) The comparison of Cone R21.5 models

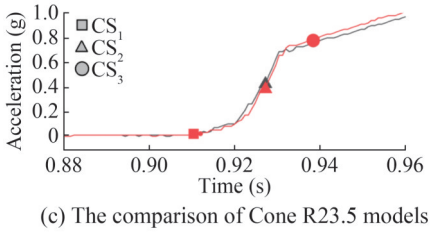

(c) The comparison of Cone R23.5 models

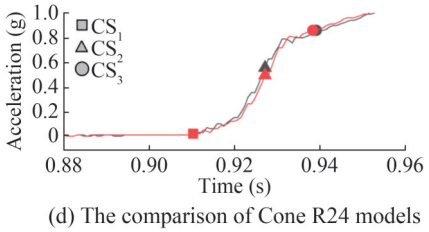

(d) The comparison of Cone R24 models

Figure 3 Comparison of the impact loads of cone models with the original mass and the same mass as the bird head model (red and black curves, respectively)

(May, 1975; Tan et al., 2016; Jiang et al., 2018a). In general, after the free fall of a model, its tip touched the water surface, which caused a slight bulge on the free water surface (Figures 5–9(a–d)). Immediately thereafter, full immersion of the largest section of the model in the water created an air–water interface (i.e., cavity formation) (Figures 5–9e). Then, continued development of the cavity was observed with the increase in entry depth, and typical water cavity flow occurred (i.e., splash, surface closure, and pinch-off of the cavity; Figures 5–9(f–k)).

Regardless of the similar water entry cavity flows observed across all experimental models, certain differences were still noticed. First, compared with the symmetrical water entry cavity of the cone models (Figures 6–9), the water entry cavity created by the bird head model was symmetrical from the front (Figures 5(a) e–i) and asymmetrical from the side (Figures 5(b) e–i) due to model asymmetry (see the Supplementary Videos S1 and S2 for further details). Moreover, the cavity size increased, and the dimensionless pinch-off time $\tau = t\sqrt{2g/d_{CS_3}}$ extended with the increase in base maximum diameter of the cone models (Tan et al., 2016) (Figures 6–9) (see Supplementary Video S3 for

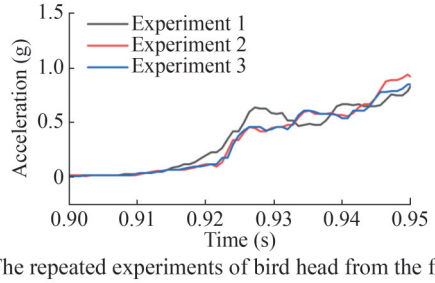

(a) The repeated experiments of bird head from the front view

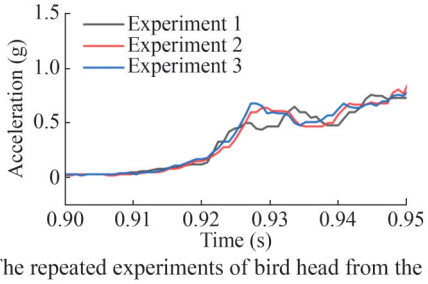

(b) The repeated experiments of bird head from the side view

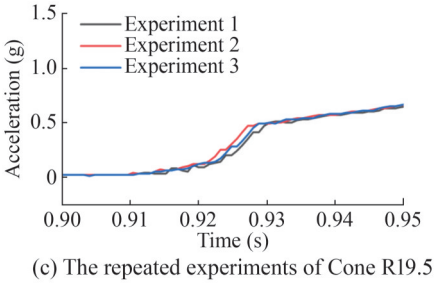

(c) The repeated experiments of Cone R19.5

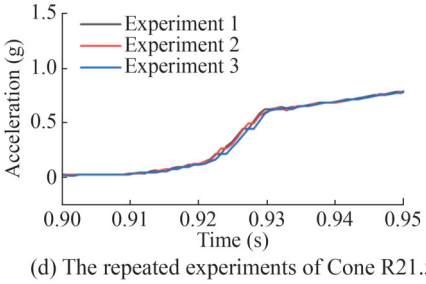

(d) The repeated experiments of Cone R21.5

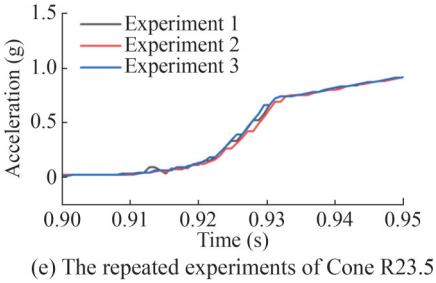

(e) The repeated experiments of Cone R23.5

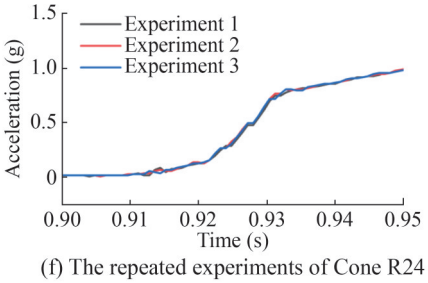

(f) The repeated experiments of Cone R24

Figure 4 Results of repeated experiments at a release height of 122 cm

further details); *t*denotes the pinch-off time. Remarkably, the bird head model showed a notably earlier dimensionless pinch-off time (Figure 5i) than all the cone models (Figures 6 – 9). Thus, the energy transfer from the entry model to the water of the bird head model was considerably smaller than that of the cone models (Jiang et al., 2021; Lee and Reddish, 1981). More specifically, previous studies on water entry cavity geometry (May, 1975) indicated that cavity geometry depends on energy transfer from the water entry model. Namely, the greater the energy transfer from the water entry model, the greater the cavity geometry (May, 1975). In addition, given its asymmetrical structure, the bird head model showed a shift in its underwater trajectory based on the side view images (Figure 5(b) k). However, the cone models maintained an almost straight line movement due to their symmetrical structure (Figures 6–9).

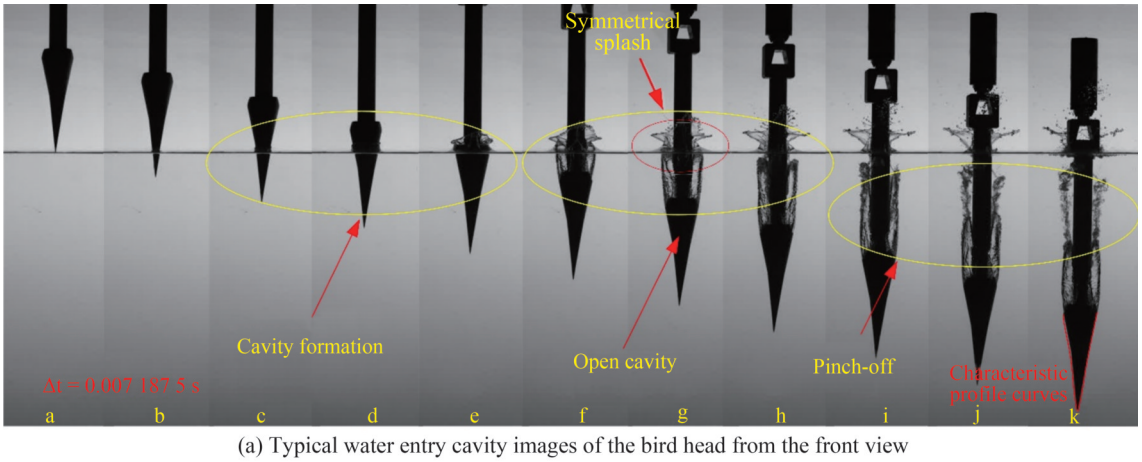

(a) Typical water entry cavity images of the bird head from the front view

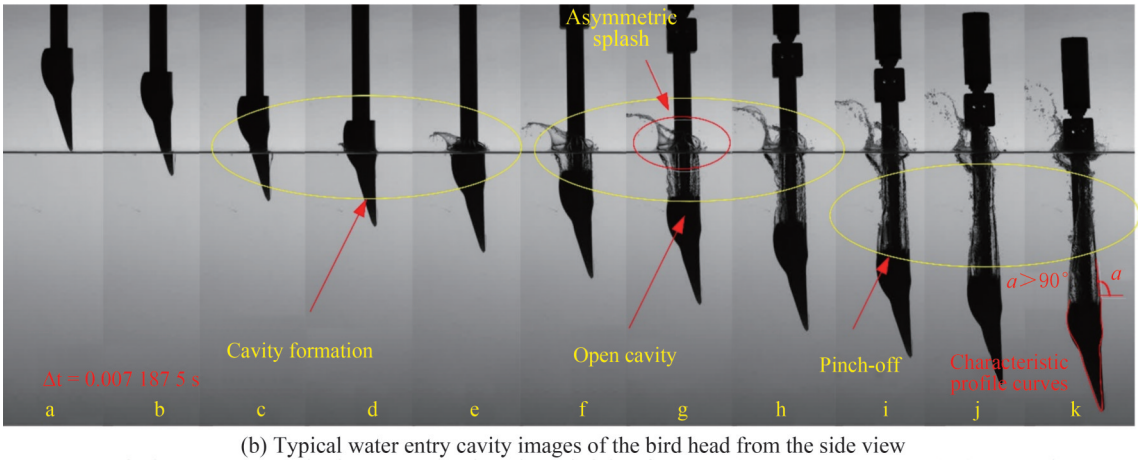

(b) Typical water entry cavity images of the bird head from the side view

Figure 5 Typical water entry cavity images under the release height of 122 cm (Fr = 7.18, τ = 1.16), (see Supplementary Videos S1 and S2 for further details, which were recorded at 6 400 frame/s and played back at 60 frame/s)

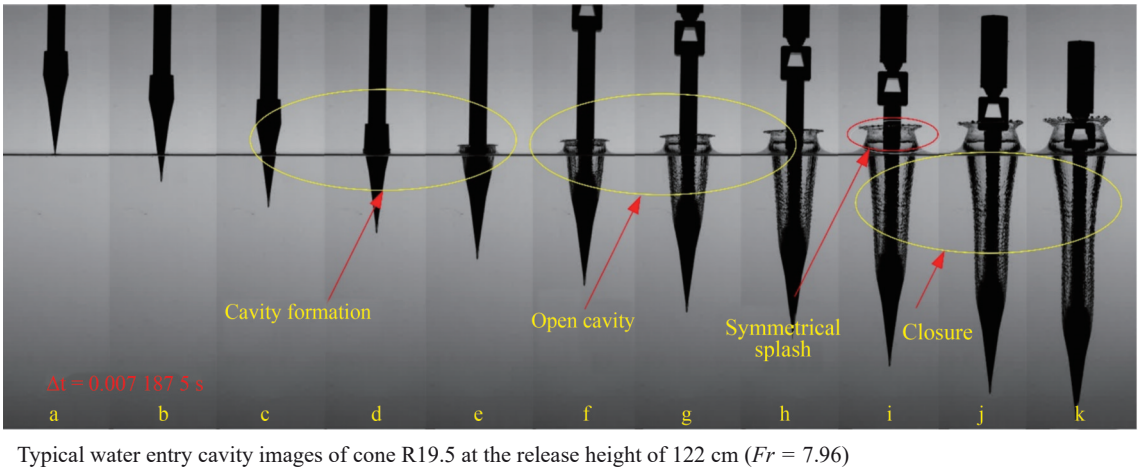

Figure 6 Typical water entry cavity images of cone R19.5 at the release height of 122 cm (Fr = 7.96)

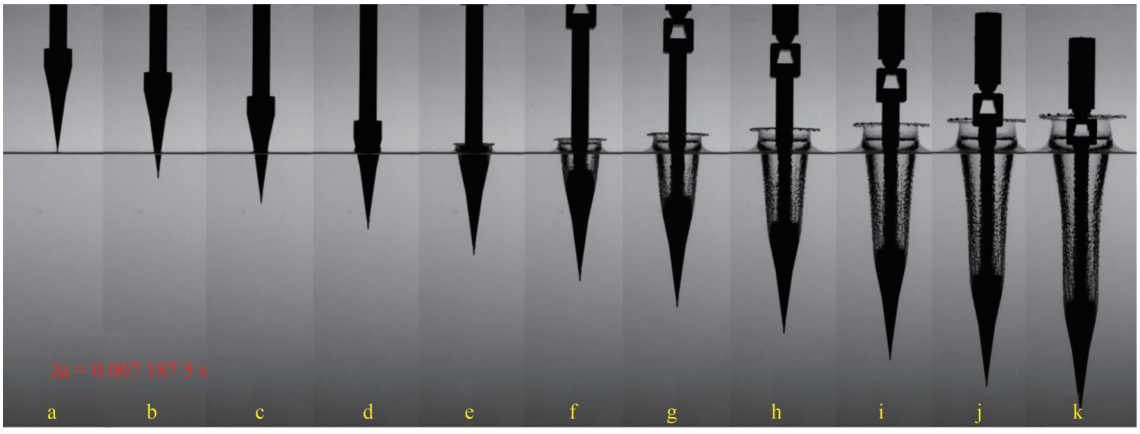

Figure 7 Typical water entry cavity images of cone R21.5 at the release height of 122 cm (Fr = 7.56)

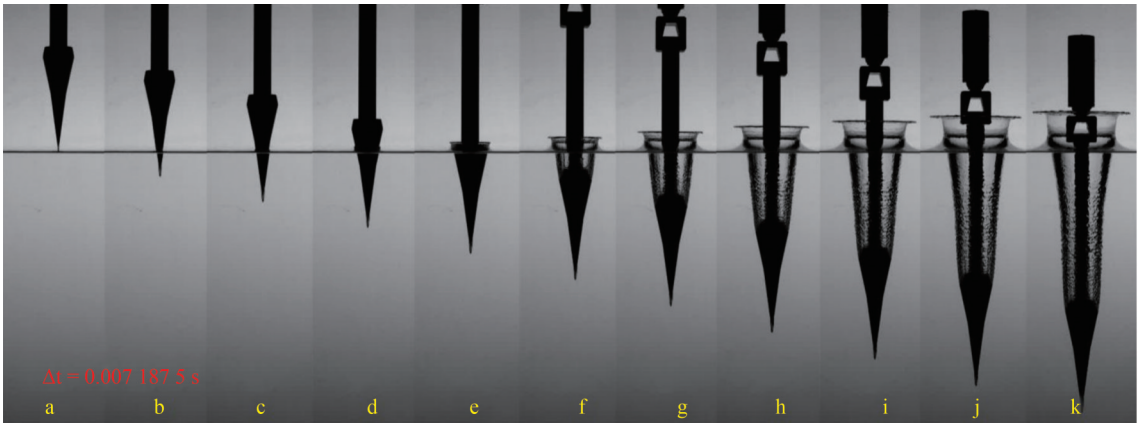

Figure 8 Typical water entry cavity images of cone R23.5 at the release height of 122 cm (Fr = 7.23) (see Supplementary Video S3 for further details, which was recorded at 6 400 frame/s and played back at 60 frame/s)

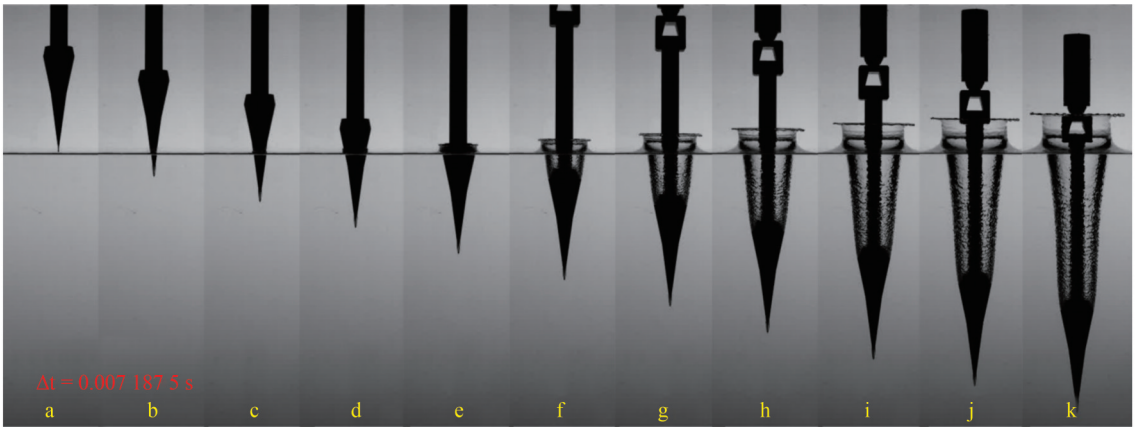

Figure 9 Typical water entry cavity images of cone R24 at the release height of 122 cm (Fr = 7.15)

To quantitatively investigate the cavity geometry across all experimental models, we measured the open-cavity diameter (D_C/D) and cavity length (L_C/D) under different entry depths, where D refers to the maximum diameter of various models. Figure 10 presents the parameter definition, and Figure 11 summarizes the results. Here, L_D refers to the depth at which the model is just submerged, and h=46.4 mm is the depth interval (Figure 10). The cavity geometry was measured based on the images captured using a high-speed camera. The cavity diameter and length observed in the images correspond to the number of pixel points. Given the relationship between camera resolution and shooting distance, the maximum measurement uncertainty of the cavity geometry was 0.34%–5.7% across all experimental conditions. As presented in Figure 11, the cavity diameter D_C and length L_C increased with the entry depth for all the cone models. However, the D_C and L_C of the bird head model suddenly decreased with the increase in entry depth

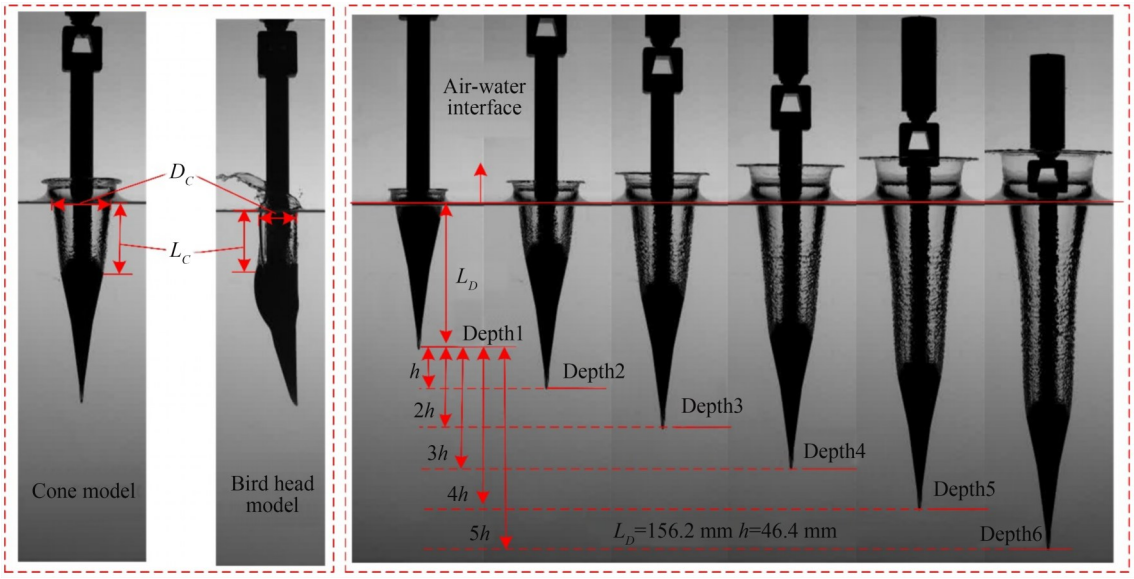

Figure 10 Definition of geometric parameters

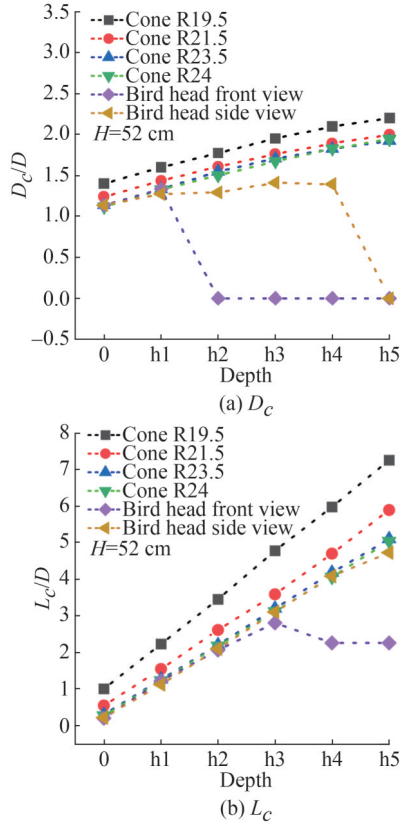

Figure 11 Cavity geometry under different entry depths for the same release height (52 cm) across all experimental models

due to the pinch-off, especially from the front view (Figure 5). In summary, the bird head model experienced a smaller splash than all the cone models and had a smaller diameter of the open cavity, which resulted in faster cavity shrinkage and rapid pinch-off. The results (images and cavity geometry) on the other two release heights (i. e., 87 cm and 122 cm) are not presented because similar trends were observed across all experimental models.

3.2 Water entry impact load

To investigate the water entry impact load characteristics of the bird head and cone models, we determined the real-time impact acceleration trends for all the models at different release heights (i.e., 122, 87, and 52 cm) (Figures 12–14).

Figure 12 shows that the tip of the bird head mode (CS_1) touched the water surface at around 0.910 4 s. Then, the impact load (upward impact acceleration) increased with the model penetration depth. The maximum cross-section (CS_3) of the bird head model entered the water at approximately 0.938 s. Although similar impact load variation trends were observed for all the cone models, the water entry impact load increased with the cone model the base maximum diameter (i. e., CS_3). Moreover, the bird head model achieved considerably lower acceleration values of water entry (0.54 g) compared with cones R24 (0.86 g), R23.5 (0.78 g), and R21.5 (0.66 g) but slightly higher values than cone R19.5 (0.53 g) (Figure 12). The impact acceleration characteristics of a bird head model at the maximum cross-section were attributed to the energy transfer characteristics from the model to water, i. e., energy transfer in the bird head was smaller than that in some cone models, as indicated by the cavity formation images in Figures 5 – 9 (May, 1975; Lee and Reddish, 1981; Jiang et al., 2021).

Similar impact load experimental results were obtained for the other two release heights (i. e., 87 cm and 52 cm) (Figures 13 and 14, respectively). At the release height of 87 cm, the water entry impact acceleration of the bird head model (0.48 g) was notably less than those for cones R24 (0.7 g), R23.5 (0.65 g), and R21.5 (0.52 g) and slightly

greater than those for cone R19.5 (0.44 g) (Figure 13). Moreover, at the release height of 52 cm, the impact acceleration of the bird head model (0.46 g) was less than that for cones R24 (0.57 g) and R23.5 (0.53 g) and was slightly greater than those for cones R21.5 (0.42 g) and R19.5 (0.35 g) (Figure 14).

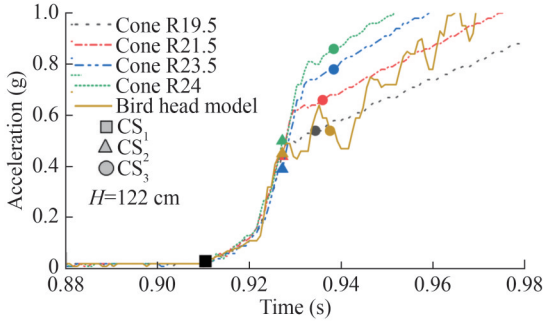

Figure 12 Water entry impact acceleration of the different models at the same release height of 122 cm (CS_1, CS_2, and CS_3 denote the rostral tip, rostral root, and maximum cross-section area, respectively)

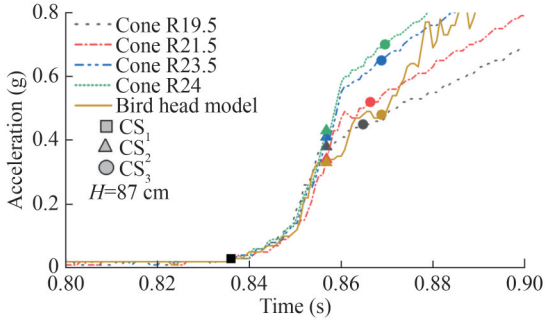

Figure 13 Water entry impact acceleration for all the models at the same release height of 87 cm

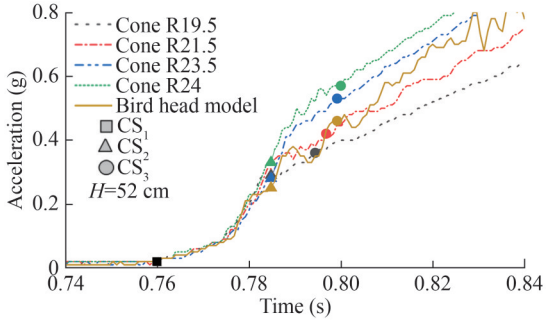

Figure 14 Water entry impact acceleration of all the models at the same release height of 52 cm

4 Conclusions

The systematic experimental investigation of the entry flow and impact load characteristics of the northern-gannet model and cone models with different maximum cross-section areas yielded noteworthy results. The model geometry topology considerably influenced the water entry cavity flow and impact load.

For the water entry flow, the northern-gannet head model created a smaller water entry splash crown and cavity geometry than similar-sized cone models. In addition, the bird head model had a remarkably earlier pinch-off time than all the cone models. The water entry flow characteristics were attributed to the unique streamlined water entry of the bird head model, which transferred a relatively small amount of energy to the water compared with the cone models. For the impact load, the bird head model attained a smaller impact acceleration at the maximum cross-section compared with similar-sized cone models (i.e., cones R24 and R23.5) across all experimental conditions. Specifically, the values of water entry acceleration observed for the bird head model (0.54, 0.48, and 0.46 g for the release heights of 112, 87, and 52 cm, respectively) were notably less than those for cones R24 and R23.5. The acceleration values for cone R24 were 0.86, 0.7, and 0.57 g, and those for cone R23.5 reached 0.78, 0.65, and 0.53 g at the mentioned release heights of 112, 87, and 52 cm).

For clarification of the physical mechanism underlying the impact acceleration of the bird head model at a maximum cross-section smaller than that of the similar-sized cone models, detailed water entry cavity flow should be measured via particle image velocimetry or numerical simulation using a suitable model.

Funding Supported by the Guangdong Provincial Natural Science Foundation of China under Grant No. 2021A1515011917, the National Natural Science Foundation of China under Grant No. 52371344 and U22A2012, Fundamental Research Funds for the Central Universities, Sun Yat-sen University under Grant No.22qntd0601, and the start-up funding to Y.J. from Sun Yat-sen University.

Competing interest The authors declare that they have no known competing financial interests or personal relationships that could have appeared to influence the work reported in this paper.

References

Bhar K, Chang B, Virot E, Straker L, Kang H, Paris R, Clanet C, Jung S (2019) How localized force spreads on elastic contour feathers. Journal of the Royal Society interface 16: 20190267. DOI: 10.1098/rsif.2019.0267

Bush JWM, Hu DL (2006) Walking on water: Biolocomotion at the interface. Annual Review of Fluid Mechanics 38: 339-369. DOI: 10.1146/annurev.fluid.38.050304.092157

Capuska GEM, Vaughn RL, Würsig B, Katzir G, Raubenheimer D (2011) Dive strategies and foraging effort in the Australasian gannet Morus serrator revealed by underwater videography. Marine Ecology Progress 442: 255-261. DOI: 10.3354/meps09458

Capuska GEM, Vaughn RL, Würsig B, Raubenheimer D (2013) Can gannets (Morus Serrator) select their diving profile prior to submergence? Notornis 60: 255-257

Chang B, Croson M, Straker L, Gart S, Dove C, Gerwin J, Jung S (2016) How seabirds plunge-dive without injuries. Proceedings

of the National Academy of Sciences-PNAS, 113: 12006-12011. DOI: 10.1073/pnas.1608628113

Clanet C, Hersen F, Bocquet L (2004) Secrets of successful stone-skipping. Nature 427: 29. DOI: 10.1038/427029a

Garthe S, Benvenuti S, Montevecchi WA (2000) Pursuit plunging by northern gannets (Sula bassana) "feeding on capelin (Mallotus villosus)". Proceedings of the Royal Society. B, Biological Sciences 267: 1717-1722. DOI: 10.1098/rspb.2000.1200

Glasheen JW, McMahon TA (1996) A hydrodynamic model of locomotion in the Basilisk Lizard. Nature (London) 380: 340-342. DOI: 10.1038/380340a0

Jiang Y, Bai T, Gao Y, Guan L (2018a) Water entry of a constraint posture body under different entry angles and ventilation rates. Ocean Engineering 153: 53-59. DOI: 10.1016/j.oceaneng.2018.01.091

Jiang, Y, Li Y, Guo J, Yang L, Wang H (2021) Numerical simulations of series and parallel water entry of supersonic. projectiles in compressible flow. Ocean Engineering 235:109155 DOI: 10.1016/j.oceaneng.2021.109155

Jiang Y, Shao S, Hong J (2018b) Experimental investigation of ventilated supercavitation with gas jet cavitator. Physics of Fluids 30: 12103. DOI: 10.1063/1.5005549

Lee DN, Reddish PE (1981) Plummeting gannets: a paradigm of ecological optics. Nature (London) 293: 293-294. DOI: 10.1038/293293a0

Liang J, Yang X, Wang T, Yao G, Zhao W (2013) Design and experiment of a bionic gannet for plunge-diving. Journal of Bionics Engineering 10: 282-291. DOI: 10.1016/S1672-6529(13)60224-3

Low KH, Hu T, Mohammed S, Tangorra J, Kovac M (2015) Perspectives on biologically inspired hybrid and multi-modal locomotion. Bioinspir & Biomim 10: 20301. DOI: 10.1088/1748-3190/10/2/020301

May A (1975) Water entry and the cavity-running behavior of missiles. NASA STI/Recon Technical Report No. 76

Pandey A, Yuk J, Chang B, Fish FE, Jung S (2022) Slamming dynamics of diving and its implications for diving-related injuries. Science Advances 8: 5888. DOI: 10.1126/sciadv.abo5888

Ropert-Coudert Y, Grémillet D, Ryan PE, Kato A, Naito Y, Maho YL (2004) Between air and water: the plunge dive of the cape gannet Morus capensis. Ibis 146: 281-290. DOI: 10.1111/j.1474-919x.2003.00250.x

Seddon CM, Moatamedi M (2006) Review of water entry with applications to aerospace structures. International Journal of Impact Engineering 32: 1045-1067. DOI: 10.1016/j.ijimpeng.2004.09.002

Sharker SI, Holekamp S, Mansoor MM, Fish FE, Truscott TT (2019) Water entry impact dynamics of diving birds. Bioinspir & Biomim 14: 56013. DOI: 10.1088/1748-3190/ab38cc

Tan BCW, Vlaskamp JHA, Denissenko P, Thomas PJ (2016) Cavity formation in the wake of falling spheres submerging into a stratified two-layer system of immiscible liquids. Journal of Fluid Mechanics 790: 33-56. DOI: 10.1017/jfm.2016.10

Truscott TT, Epps BP, Belden J (2014) Water entry of projectiles. Annual Review of Fluid Mechanics 46: 355-378. DOI: 10.1146/annurev-fluid-011212-140753

Wang TM, Yang XB, Liang JH, Yao GC, Zhao WD (2013) CFD based investigation on the impact acceleration when a gannet impacts with water during plunge diving. Bioinspir & Biomim 8: 36006. DOI: 10.1088/1748-3182/8/3/036006

Yang X, Wang T, Liang J, Yao G, Chen Y, Shen Q (2012) Numerical analysis of biomimetic gannet impacting with water during plunge-diving. IEEE International Conference on Robotics & Biomimetics: 569-574. DOI: 10.1109/ROBIO.2012.6491027

Zimmerman S, Ceballes S, Taylor G, Chang B, Jung S, Abdelkefi A (2019) Nonlinear modeling and experimental verification of gannet-inspired beam systems during diving. Bioinspir & Biomim 14: 26002. DOI: 10.1088/1748-3190/aaf98c

Zimmerman S, Abdelkefi A (2020a) Enhanced design considerations on the buckling and dynamics of gannet-inspired systems during water entry. Bioinspir & Biomim 16: 26011. DOI: 10.1088/1748-3190/abc468

Zimmerman S, Abdelkefi A (2020b) Investigations on the buckling and dynamics of diving-inspired systems when entering water. Bioinspir & Biomim 15: 36015. DOI: 10.1088/1748-3190/ab76d8